MISSOURI S&T

Missouri University of Science and Technology

Scholars' Mine

Electrical and Computer Engineering Faculty
Research & Creative Works

Electrical and Computer Engineering

Radiation Imaging Operators Applied to the Detection of Velocity and Density Contrast Boundaries

Md. Ishfaqur Raza

Richard E. DuBroff
Missouri University of Science and Technology, red@mst.edu

James L. Drewniak
Missouri University of Science and Technology, drewniak@mst.edu

Follow this and additional works at: https://scholarsmine.mst.edu/ele_comeng_facwork

Part of the Electrical and Computer Engineering Commons

Recommended Citation

M. I. Raza et al., "Radiation Imaging Operators Applied to the Detection of Velocity and Density Contrast Boundaries," *IEEE Transactions on Ultrasonics, Ferroelectrics and Frequency Control*, vol. 44, no. 6, pp. 1401-1404, Institute of Electrical and Electronics Engineers (IEEE), Nov 1997.
The definitive version is available at https://doi.org/10.1109/58.656644

Correspondence _____

Radiation Imaging Operators Applied to the Detection of Velocity and Density Contrast Boundaries

Md. Ishfaqur Raza,
Richard E. DuBroff, *Senoir Member, IEEE*,
and James L. Drewniak, *Member, IEEE*

Abstract—A procedure for imaging interfaces formed by simultaneous density and velocity contrasts in acoustic media is described. The procedure is based on the properties of radiation imaging operators—a class of linear differential operators parametrically dependent on the acoustic properties of the media. An example of this procedure is demonstrated through the use of numerical simulation. Results, in the form of interface images, are shown, assuming the bulk acoustic characteristics (velocity and density) on both sides of the interface are known.

I. INTRODUCTION

T HE OBJECTIVE of this investigation is to reconstruct the images of acoustic interfaces formed by simultaneous velocity and density contrasts. In [1], radiation imaging operators were introduced as the basis of a nondestructive imaging technique to detect acoustic interfaces between materials having different acoustic velocities. In this paper, the approach is extended to take into consideration materials having contrasting densities as well.

Input data for this procedure consists of a set of spatially and temporally sampled values of the total acoustic wave (incident and scattered) produced by one or more known sources placed at known locations. The spatial sampling corresponds to a number of acoustic sensors located at discrete points on a reference (datum) surface, as shown in Fig. 1. This datum surface resides entirely in medium 1. Further description of Fig. 1 will be given in Section II.

The technique presented here uses a radiation imaging operator (RIO) based on a second order radiation boundary condition (RBC) combined with material boundary conditions satisfied at the interface, as in [1]. The RBCs were introduced by Engquist and Majda [2] in 1977. A general discussion on RBCs and some of their subsequent applications can be found in [3].

II. CONSTRUCTING THE RADIATION IMAGING OPERATOR

Fig. 1 shows an interface between two acoustic media, each in the form of a semi-infinite half space. The unit vectors $\hat{n}$ and $\hat{\tau}$ denote the normal and tangential directions at each point along the interface. The half spaces are characterized by acoustic velocities of c_1 and c_2, respectively. The mass densities of the
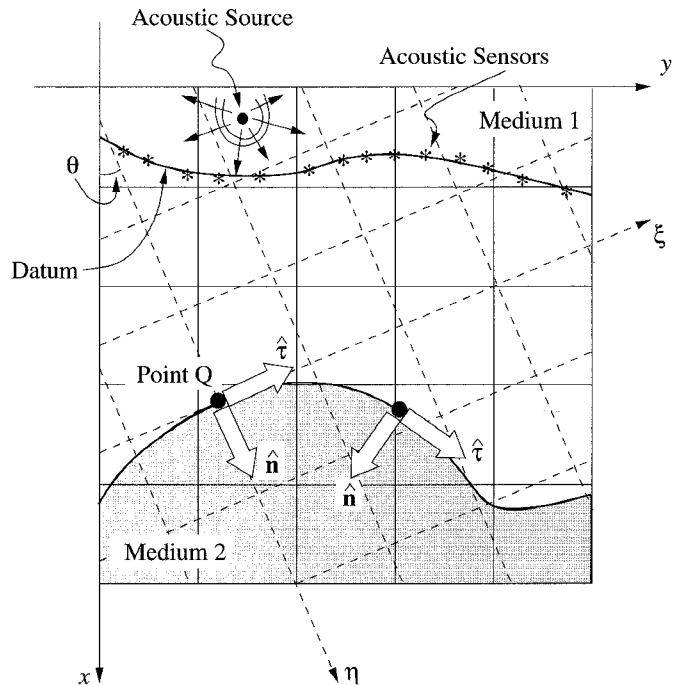
Fig. 1. The computational (xy) and boundary oriented ($\eta\xi$) coordinate systems.

two media are ρ_1 and ρ_2. The xy coordinate system is chosen as any convenient computational coordinate system, selected without regard for the orientation of the boundary between the two media. The $\eta\xi$ coordinate system is a boundary oriented coordinate system, chosen so that the boundary normal at point Q, an arbitrary point on the interface, is entirely in the η direction. The variable s refers to arclength measured along the interface. Arclength is arbitrarily defined to increase in the direction of increasing τ. The designation of point Q as the origin of the $\eta\xi$ coordinate system (as shown in Fig. 1) is not strictly necessary provided the η and ξ axes are, respectively, perpendicular and tangential to the boundary at point Q.

As noted in [1], a second order RBC for a wave propagating in the η direction into the interior of Medium 2 at point Q can be written as:

$$\left\{ c_2 \partial_{\eta t}^2 + \partial_{tt}^2 - \frac{1}{2} c_2^2 \partial_{\xi\xi}^2 \right\} p_2 \left(\mathbf{r}, t \right) \Big|_Q \simeq 0. \tag{1}$$

Converting this RBC into a usable radiation imaging operator then consists of two steps. First, all of the partial derivatives acting upon $p_2 \left(\mathbf{r}, t \right)$ need to be converted into partial derivatives acting upon $p_1 \left(\mathbf{r}, t \right)$ since the observed data is presumed to consist of a set of sampled values of $p_1 \left(\mathbf{r}, t \right)$ rather than a set of sampled values of $p_2 \left(\mathbf{r}, t \right)$. Second, partial differentiation in the boundary oriented coordinate system ($\eta\xi$) needs to be transformed into partial differentiation in the computational coordinate system (xy).

The conversion procedure begins with the acoustic material boundary conditions (MBCs) satisfied at the interface expressing continuity of pressure and continuity of the normal compo-

nent of displacement:

$$p_2(\mathbf{r}, t) = p_1(\mathbf{r}, t) \quad \text{and} \quad \frac{\partial}{\partial n} p_2(\mathbf{r}, t) = \gamma \frac{\partial}{\partial n} p_1(\mathbf{r}, t).$$
$$(2)$$

Letting s represent arclength measured along the interface; assuming that the pressure functions, $p_1(\mathbf{r}, t)$ and $p_2(\mathbf{r}, t)$ at point Q, are continuously differentiable up to the second order; and assuming that the interface is sufficiently smooth, MBCs in (2) can be written as:

$$\left.\frac{\partial^k}{\partial t^k} p_2(\mathbf{r}, t)\right|_Q = \left.\frac{\partial^k}{\partial t^k} p_1(\mathbf{r}, t)\right|_Q \quad \text{for } k = 0, 1, 2 \qquad (3)$$

$$\left.\frac{\partial^{k+1}}{\partial t^k \partial \eta} p_2(\mathbf{r}, t)\right|_Q = \left.\gamma \frac{\partial^{k+1}}{\partial t^k \partial \eta} p_2(\mathbf{r}, t)\right|_Q \quad \text{for } k = 0, 1 \qquad (4)$$

$$\left.\frac{\partial^k}{\partial s^k} p_2(\mathbf{r}, t)\right|_Q = \left.\frac{\partial^k}{\partial s^k} p_1(\mathbf{r}, t)\right|_Q \quad \text{for } k = 0, 1, 2 \qquad (5)$$

where γ represents the mass density ratio (ρ_2/ρ_1). Furthermore, as shown in Fig. 1, the ξ direction is tangential to the interface at point Q. Therefore,

$$\left.\frac{d\eta}{ds}\right|_Q = 0 \quad \text{and} \quad \left.\frac{d\xi}{ds}\right|_Q = 1. \qquad (6)$$

When (3) through (6) are used to express the partial derivatives of $p_2(\mathbf{r}, t)$ evaluated at point Q in terms of partial derivatives of $p_1(\mathbf{r}, t)$, (1) becomes:

$$\left\{ c_2 \gamma \partial_{\eta t}^2 + \partial_{tt}^2 - \frac{1}{2} c_2^2 \left[\partial_{\xi\xi}^2 + (1 - \gamma) \frac{d^2\eta}{ds^2} \partial_\eta \right] \right\} p_1(\mathbf{r}, t) \Bigg|_Q \simeq 0. \qquad (7)$$

Transforming the independent variables, η and ξ, into the computational coordinates, x and y, finally yields the following condition on $p_1(\mathbf{r}, t)$ at point Q:

$$\left\{ c_2 \gamma \left[n_x \partial_{xt}^2 + n_y \partial_{yt}^2 \right] + \partial_{tt}^2 - \frac{1}{2} c_2^2 \left[n_y^2 \partial_{xx}^2 - 2n_x n_y \partial_{xy}^2 \right. \right.$$

$$\left. + n_x^2 \partial_{yy}^2 \right] - \frac{1}{2} c_2^2 (1 - \gamma) \frac{d^2\eta}{ds^2} \left[n_x \partial_x + n_y \partial_y \right] \right\} p_1(\mathbf{r}, t) \Bigg|_Q \simeq 0. \qquad (8)$$

The partial differential operator in (8) is a RIO. The operator depends upon the values of the parameters c_2, γ, n_x, and $\frac{d^2\eta}{ds^2}$ at point Q. The parameter n_y is not an independent parameter because $n_x^2 + n_y^2$ must equal 1. Using the notation $\mathcal{L}_{\text{RIO}}\left(c_2, \gamma, n_x, \frac{d^2\eta}{ds^2} \right)$ to refer to this differential operator, it is possible to define an image function, $\mathcal{I}(\mathbf{r})$, at each point in space as the time averaged absolute value of the left side of (8), that is:

$$\mathcal{I}(\mathbf{r}) \equiv \left\langle \left| \mathcal{L}_{\text{RIO}}\left(c_2, \gamma, n_x, \frac{d^2\eta}{ds^2} \right) p_1(\mathbf{r}, t) \right| \right\rangle_t. \qquad (9)$$

III. NUMERICAL RESULTS

The proposed imaging procedure, based on (9), was tested using data generated by a finite-difference time-domain (FDTD) algorithm [4], [5] applied to the two-dimensional model
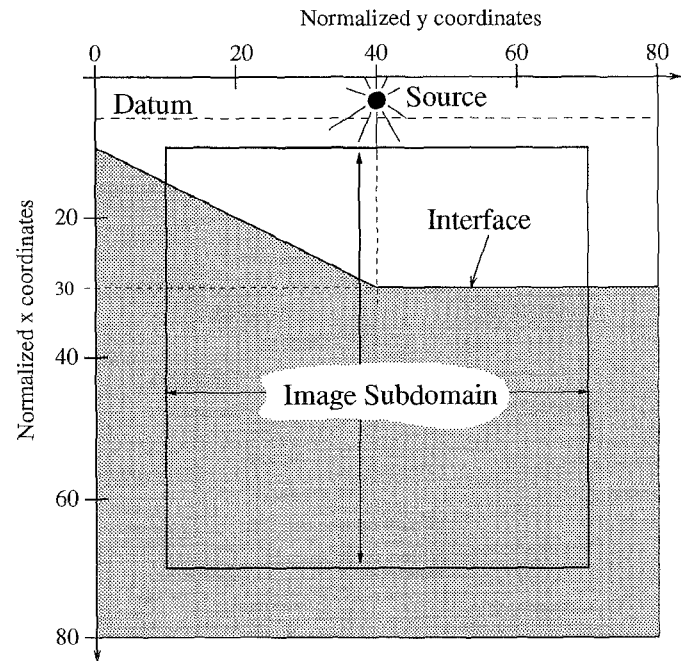

Fig. 2. An interface separating two acoustic media.

shown in Fig. 2. The spatial computational grid for the FDTD algorithm consisted of 81 computational nodes in the x direction by 81 computational nodes in the y direction, and the record length was 800 time steps. The simulated acoustic source consisted of a line source, located at $(X, Y) = (3, 40)$ where X and Y represent the x and y coordinates normalized by the sampling intervals, δ_x and δ_y, respectively. The source signature function was a Gaussian pulse in the form of:

$$s(t) = \exp\left[-\frac{(t - t_0)^2}{\tau^2} \right]$$

with $t_0 = 11.9$ msec and $\tau = 5.1$ msec. At the 20 dB bandwidth of this signature function, the computational grid shown in Fig. 2 is approximately 9 wavelengths long on each side. For each of the 81 computational nodes on the datum surface $(Y = 0$ to 80 for $X = 5)$, the FDTD algorithm yielded a set of 801 consecutive time samples of the total acoustic pressure, $p_1(\mathbf{r}, t)$. These sampled values of the total acoustic pressure on the datum surface constitute the input for the imaging procedure.

A schematic diagram of the imaging procedure is shown in Fig. 3. In this diagram the data obtained from the FDTD algorithm is shown in Block 0. The value of the incident wave $(p_i(\mathbf{r}, t)$ as shown in Block 1) can, in many cases involving simple sources, be calculated analytically or, alternatively, it can be calculated numerically. The latter approach was used in this case. Subtracting the values of the incident wave at the datum from the corresponding values of the total acoustic wave at the datum yields the scattered wave at the datum $(p_s(\mathbf{r}, t)|_{S_0}$ as shown in Block 2; S_0 indicates the datum). By applying the FDTD algorithm in reverse time [6], [7], the values of the scattered wave at points below the datum can then be calculated $(p_s(\mathbf{r}, t)$ in Block 3). The incident and scattered waves at points below the datum can then be recombined to produce the total acoustic wave $(p_1(\mathbf{r}, t)$ in Block 4) at points below the datum. The final step then consists of forming the image
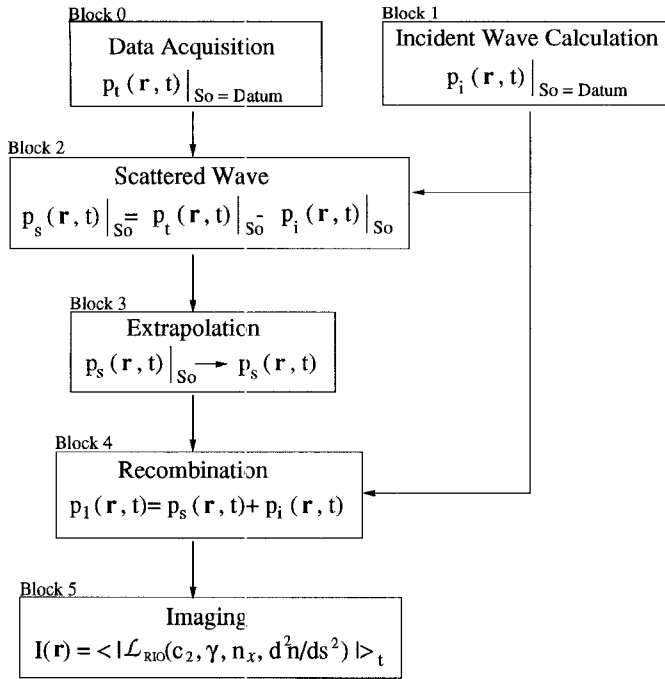
Block 0
Data Acquisition
$$p_t(\mathbf{r}, t)\big|_{So\,=\,Datum}$$

Block 1
Incident Wave Calculation
$$p_i(\mathbf{r}, t)\big|_{So\,=\,Datum}$$

Block 2
Scattered Wave
$$p_s(\mathbf{r}, t)\big|_{So} = p_t(\mathbf{r}, t)\big|_{So} - p_i(\mathbf{r}, t)\big|_{So}$$

Block 3
Extrapolation
$$p_s(\mathbf{r}, t)\big|_{So} \longrightarrow p_s(\mathbf{r}, t)$$

Block 4
Recombination
$$p_1(\mathbf{r}, t) = p_s(\mathbf{r}, t) + p_i(\mathbf{r}, t)$$

Block 5
Imaging
$$I(\mathbf{r}) = <|\mathcal{L}_{RIO}(c_2, \gamma, n_x, d^2\eta/ds^2)|>_t$$

Fig. 3. Flowchart of imaging procedure.

Fig. 4. Normalized image function output.

function, $\mathcal{I}(\mathbf{r})$, as shown in Block 5. The partial derivatives in $\mathcal{L}_{RIO}$ are all evaluated using finite-difference approximations.

The resulting image function for the model shown in Fig. 2 was calculated and is displayed in Fig. 4. The range of values of the image function has been normalized by dividing the actual value of the image function by its maximum value over all points in the image subdomain. In calculating this image, the correct values of c_2 and γ ($c_2 = 2000$ m/s and $\gamma = 2$) were used in (9). The curvature of the interface ($\frac{d^2\eta}{ds^2}$) was assumed to be equal to zero everywhere. The x and y components of the boundary normal direction (n_x and n_y) were assumed to be 1 and 0, respectively.

In Fig. 4, the interface corresponds to a region of relatively small values of the image function. The contrast between this region and the rest of the image can be enhanced by using standard image processing techniques (e.g., [8]). The Laplacian operator, for example, when applied to a discretized image function with equal sampling intervals in the x and y directions yields a new image function, $\mathcal{I}'_{X,Y}$, where

$$\mathcal{I}'_{X,Y} = \frac{4}{\delta_x^2}\left[\frac{\mathcal{I}_{X+1,Y} + \mathcal{I}_{X,Y-1} + \mathcal{I}_{X,Y-1} + \mathcal{I}_{X,Y+1}}{4} - \mathcal{I}_{X,Y}\right]. \tag{10}$$

As can be seen from (10), the new image function provides a measure of the difference between the image intensity at one pixel and the average of the image intensities at neighboring pixels. The enhanced contrast in the new image function is shown in Fig. 5. One readily available measure of the error in this image is to consider, for each value of Y between 10 and 70, the vertical displacement between the true position of the interface (in Fig. 2) and the value of X at which $\mathcal{I}'_{X,Y}$ attains its maximum value. Applying this criteria to the image in Fig. 5, the maximum vertical error in locating the interface is less than 0.6 wavelengths and occurs near the point where the interface changes slope. A slightly smaller error (about 0.5 wavelengths) occurs as the right edge o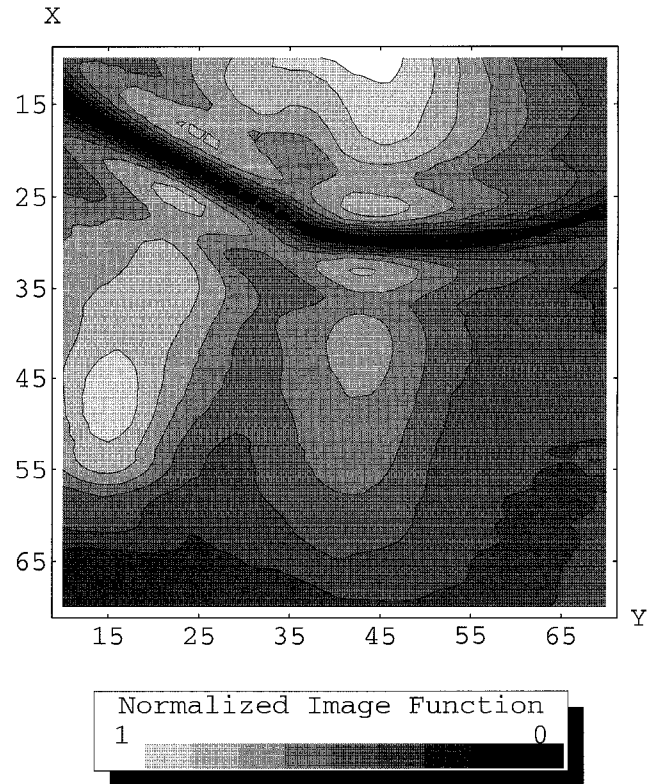f the image is approached. With the exception of the intervals $56 \leq Y \leq 70$ and $30 \leq Y \leq 51$, the vertical error is less than one spatial sampling interval.

IV. CONCLUSIONS

The accuracy of this proposed imaging technique depends upon several factors. Some of these factors, such as the effect of finite aperture width [9], are well-known and are common to many different imaging techniques. In addition, there are a number of other factors which are particularly significant in the use of radiation imaging operators.

For example, neglecting the boundary curvature term, $-(1/2)c_2^2\left(d^2\eta/ds^2\right)[n_x\partial_x + n_y\partial_y]$, in (8) would be justified when the interface is known to be flat. More generally, by comparing the terms

$$c_2\gamma\partial_{\eta t}^2 p_1(\mathbf{r}, t) \quad \text{and} \quad -\frac{1}{2}c_2^2(1-\gamma)\frac{d^2\eta}{ds^2}\partial_\eta p_1(\mathbf{r}, t)$$

it can be shown [4] that for a time harmonic wave

$$\left|c_2\gamma\partial_{\eta t}^2 p_1(\mathbf{r}, t)\right| \gg \left|-\frac{1}{2}c_2^2(1-\gamma)\frac{d^2\eta}{ds^2}\partial_\eta p_1(\mathbf{r}, t)\right|$$

when the radius of curvature of the boundary is large compared to $\frac{\gamma-1}{\gamma}$ times the wavelength. Under this condition the
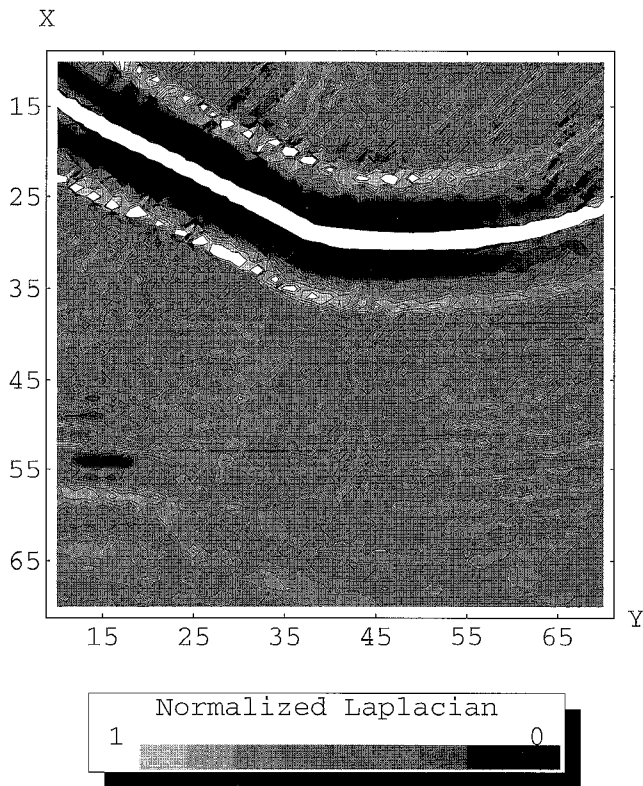
Fig. 5. Normalized Laplacian of the image function output.

curvature of the interface can be neglected. In the case of the interface shown in Fig. 2, this condition is obviously not satisfied at the point where the slope of the interface changes abruptly.

The use of an incorrect value for the angle θ as shown in Fig. 1, corresponding to incorrect values for the parameters n_x and n_y, is another potential source of error. In obtaining the images shown in Figs. 4 and 5, the angle θ was assumed to be $0°$, i.e., $n_x = 1$ and $n_y = 0$, uniformly throughout the image subdomain. An incorrect selection for n_x and n_y affects the image quality in two ways.

First, the second order RBC, (1), used in the construction of the radiation imaging operator is satisfied exactly for a plane wave propagating in the boundary normal direction. For plane waves propagating in other directions, this RBC is only satisfied approximately [3], [10]. Second, an incorrect choice for this angle introduces errors in the formulas [such as (4)] used to relate the derivatives of $p_2(\mathbf{r}, t)$ to the derivatives of $p_1(\mathbf{r}, t)$. Nevertheless, the results given in Figs. 4 and 5 show that this imaging method can accommodate some degree of misalignment between the assumed values of n_x and n_y and their correct values. Specifically, for the inclined portion of the interface in Fig. 2, the correct values of n_x and n_y were $\cos\left(26.6°\right)$ and $-\sin\left(26.6°\right)$. However, the inclined portion of the interface is still clearly visible in Figs. 4 and 5, even when (9) used $n_x = 1$ and $n_y = 0$ uniformly throughout the image subdomain.

Possible extensions of this approach include reformulating the radiation imaging operators to utilize different types of RBCs. The second order RBC given in (1) generally introduces small errors when the acoustic pressure, $p_2(\mathbf{r}, t)$ is not a plane wave propagating in the boundary normal direction. Other types of RBCs, such as PML [11], could potentially reduce this source of error. Preliminary attempts to determine the values of γ, c_2, and $\frac{d^2\eta}{ds^2}$ by applying least squares optimization to (9) have, so far, been unsuccessful; part of the difficulty may be due to the inherent limitations of the underlying RBC used in (1). Radiation boundary conditions of higher order [12] might also be useful in extending this method to allow for the determination of parameters in the second medium. Unfortunately many of the higher order RBCs require the numerical evaluation of higher order derivatives and this, in turn, may significantly increase the computational burden required to generate images using this approach.

One possible advantage of extending this approach to interfaces in three spatial dimensions concerns the finite-difference time-domain extrapolation process for the scattered waves. As in [1], the final conditions used for this type of extrapolation assumed that the incident and scattered wavefields had become negligible at the end of each record (i.e., after 801 time steps). Due to the dispersive nature of two-dimensional wave propagation [13], this assumption is more easily met in three spatial dimensions.

REFERENCES

[1] R. E. DuBroff, M. I. Raza, and T. J. Herrick, "Remote detection of acoustic boundaries using radiation imaging operators," *IEEE Trans. Ultrason., Ferroelect., Freq. Contr.*, vol. 42, pp. 1012–1019, Nov. 1995.
[2] B. Engquist and A. Majda, "Absorbing boundary conditions for the numerical simulation of wave," *Math. Comput.*, vol. 31, pp. 629—651, July 1977.
[3] T. G. Moore, J. G. Blaschak, A. Taflove, and G. A. Kriegsmann, "Theory and application of radiation boundary operators," *IEEE Trans. Antennas Propagat.*, vol. AP-36, pp. 1979–1812, Dec. 1988.
[4] M. I. Raza, "Remote detection of interfaces using radiation imaging operators," Ph.D. dissertation, Department of Electrical Engineering, Univ. Missouri-Rolla, 1997.
[5] X. Zhang and K. K. Mei, "Time-domain finite-difference approach to the calculation of the frequency-dependent characteristics," *IEEE Trans. Microwave Theory Tech.*, vol. MTT-36, pp. 1775–1787, Dec. 1988.
[6] G. A. McMechan, "Determination of source parameters by wavefield extrapolation," *Geophys. J. Royal Astr. Soc.*, vol. 71, pp. 613–628, 1982.
[7] J. F. Claerbout, *Fundamentals of Geophysical Data Processing.* New York: McGraw-Hill, 1976.
[8] B. K. Horn, *Robot Vision.* Cambridge, MA: MIT Press, 1986.
[9] A. J. Berkhout, *Seismic Migration—Image of Acoustic Energy by Wavefield Extrapolation. Part B. Practical Aspects.* New York: Elsevier Sci. Publishers, 1985.
[10] W. C. Chew, *Waves and Fields in Inhomogeneous Media.* New York: Van Nostrand Reinhold, 1990.
[11] J. P. Berenger, "A perfectly matched layer for the absorption of electromagnetic waves," *J. Comput. Phys.*, vol. 114, pp. 185–200, 1994.
[12] R. L. Higdon, "Absorbing boundary conditions for difference approximations to the multi-dimensional wave equation," *Math. Comput.*, vol. 47, pp. 437–459, Oct. 1986.
[13] P. M. Morse and H. Feshbach, *Methods of Theoretical Physics.* New York: McGraw-Hill, 1953.